ELSEVIER

Deep-Sea Research II 51 (2004) 2889–2904

DEEP-SEA RESEARCH
PART II

www.elsevier.com/locate/dsr2

Internal wave excitation from a collapsing mixed region

B.R. Sutherland*, M.R. Flynn, K. Dohan

Department of Mathematical and Statistical Sciences, University of Alberta, Edmonton, Alta., Canada T6G 2G1

Abstract

The collapse of a uniform density fluid (a "mixed region") into a surrounding ambient fluid with complex stratification is examined by way of laboratory experiments and fully nonlinear numerical simulations. The analysis focuses upon the consequent generation of internal gravity waves and their influence upon the evolution of the collapsing mixed region. In experiments and simulations for which the ambient fluid has uniform density over the vertical extent of the mixed region and is stratified below, we find the mixed region collapses to form an intrusive gravity current and internal waves are excited in the underlying stratified fluid. The amplitude of the waves is weak in the sense that the intrusion is not significantly affected by the waves. However, scaling the results to the surface mixed layer of the ocean we find that the momentum flux associated with the waves can be as large as $1\,\mathrm{N/m^2}$. In simulations for which the ambient fluid is stratified everywhere, including over the vertical extent of the mixed region, we find that internal waves are excited with such large amplitude that the collapsing mixed region is distorted through strong interactions with the waves.

1. Introduction

Internal gravity waves (hereafter "IGW") transport energy and momentum vertically through such density stratified fluids as the atmosphere and ocean. IGW generated by flow over topography exert a drag where they break at upper levels in the atmosphere. However, it is only recently that the importance of breaking IGW for transport processes in the near-surface and abyssal ocean has been appreciated.

In the equatorial Pacific, for example, the vertically integrated zonal pressure gradient approximately balances the surface zonal wind stress over seasonal or annual time scales. However, Dillon et al. (1989) have demonstrated that over short time scales the zonal pressure gradient, mesoscale eddy flux and advection cannot be balanced by turbulent stress divergence alone. It was subsequently suggested by Wijesekera and Dillon (1991) and Hebert et al. (1991) that the momentum transported by dynamically generated IGW accounts for this disparity.

*Corresponding author. Tel.: +1 780 492 0573; fax: +1 780 492 6826.

E-mail address: bruce.sutherland@ualberta.ca (B.R. Sutherland).

0967-0645/$ - see front matter © 2004 Elsevier Ltd. All rights reserved.
doi:10.1016/j.dsr2.2004.09.002

Some of the mechanisms for IGW generation below the surface mixed layer which have been investigated through observations, experiments and simulations include dynamic (Kelvin–Helmholtz) instability, turbulent eddies and the "obstacle effect" (e.g. see Moum et al., 1992; Skyllingstad and Denbo, 1994; Sutherland, 1996; Smyth and Moum, 2002; Dohan and Sutherland, 2003). The last of these mechanisms describes wave excitation by the relative horizontal flow of the thermocline underneath the deformed base of the surface mixed layer where the deformation occurs, for example, due to convective plumes or Langmuir circulations. This mechanism is dynamically similar to topographic forcing in which the plumes act as obstacles to a stratified flow.

In the deep ocean, flow over rough bathymetry is perhaps the most important global mechanism for IGW excitation. In particular, observations in the Brazil Basin indicate that IGW generated by barotropic tidal motions over the rough bottom topography of the Mid-Atlantic Ridge are responsible for much of the observed mixing in the region (e.g. Ledwell et al., 2000; St. Laurent et al., 2001). In light of this result, present theories of the global ocean circulation are being revised. It is no longer assumed that the upwelling branch of the thermohaline circulation is a slow diffusive process but rather involves rapid and localized mixing processes that, as yet, are poorly understood.

There are three mechanisms for IGW generation by topographic forcing being actively researched at present: through interaction with bottom topography the barotropic tide may create internal tides (Smith and Young, 2002; Balmforth et al., 2002); quasi-steady flow over topography may generate internal lee waves (e.g. Garrett and St. Laurent, 2002; Sutherland, 2002); and flow near rough topography generates turbulence, which in turn may excite IGW (Sutherland and Linden, 1998; Dohan and Sutherland, 2003).

The last mechanism is particularly complex because IGW can be generated both through interactions with eddies as the turbulent mixed patch develops and through the collapse of the mixing region into the surrounding stratified fluid. This paper aims to elucidate the dynamics governing the collapse of uniform fluid into a stratified ambient and the consequent generation of IGW.

Although this research has been motivated by an oceanographic example, the generic nature of the research allows it to be adapted to a broad range of geophysical circumstances including wave generation due to convective mixing at an atmospheric inversion and wave generation in the stratosphere resulting from high-level thunderstorm outflows.

For example, Fig. 1A schematically represents a circumstance whereby the top of a severe storm spreads horizontally under the tropopause. In addition to the many well-studied mechanisms

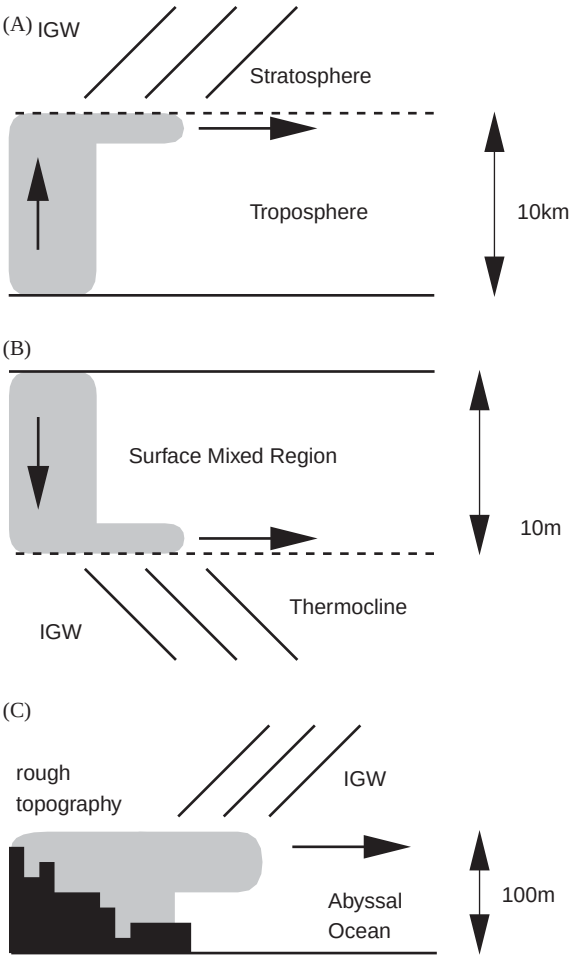

Fig. 1. Schematic showing possible mechanisms for IGW generation in the atmosphere and ocean.

for convective-generation of IGW (Beres et al., 2002; Michaelian et al., 2002) the novel mechanism illustrated here shows IGW excitation in the stratosphere as a result of the horizontal propagation of air moving underneath this stratified region (Flynn and Sutherland, 2004).

Conversely we can imagine an oceanographic circumstance, depicted in Fig. 1B, in which an intrusion moves along the top of the thermocline generating downward propagating IGW. Due to lack of observational data, we can only hypothesize the source of the intrusion; possibly it results from intense localized surface cooling or from storm-induced mixing that extends into the thermocline (Cornillon et al., 1987; Price et al., 1994). It is beyond the scope of this work to examine the origins of the intrusion. Rather we presume that it exists and that it propagates along the thermocline. One goal of this paper is to quantify some aspects of the coupling between this intrusion and the IGW generated in the underlying stratified fluid.

This is an original study in two senses. First, whereas most existing research into intrusions has examined their propagation either in a two-layer or in a uniformly stratified fluid, here we study the hybrid case of an intrusion in a two-layer fluid in which the upper layer has uniform density and the lower layer is uniformly stratified. The first detailed experimental investigation was performed by Flynn and Sutherland (2004), the results of which are adapted to oceanographic circumstances here and are complemented by numerical simulations. Second, whereas most studies of intrusions and gravity currents (which propagate along a horizontal boundary) have analyzed their propagation speeds and mixing efficiencies, here we focus upon the generation of IGW and upon the interaction between these waves and the intrusion.

Geophysical motivation for the study of these interactions is represented by a third scenario shown in Fig. 1C. Here, we imagine that mixing near rough topography in the ocean (whether due to the motion of stratified fluid over a rough surface or due to wave breaking) generates a uniform patch of fluid that collapses to form an intrusion. From the point of view of this study, the important difference between the scenarios in Figs. 1B and C is that the intrusion in the former case propagates primarily within a uniform-density ambient (the surface mixed layer) whereas in the latter case it propagates in a stratified ambient. We will demonstrate that the evolution of the intrusion and the IGW it generates is qualitatively different in these two scenarios.

In Section 2 we describe the setup of laboratory experiments and compare it with the setup of experiments by Maxworthy et al. (2002), who recently studied bottom-propagating currents in uniformly stratified fluid. The experimental results are presented in Section 3. In Section 4 we describe the numerical code used to simulate dynamics close to experimental conditions and their extension to circumstances that cannot be attained in the laboratory. Section 5 directly compares the numerical and experimental results. This section also compares simulations of mixed regions collapsing in a uniformly stratified ambient fluid with those collapsing in a uniform density fluid having an underlying stratified region. In Section 6 we apply our experimental results to a hypothetical situation in which IGW are generated by an intrusion in the ocean's surface mixed layer. Finally, we summarize our results in Section 7.

2. Experimental setup and analyses

Intrusive gravity currents in uniformly stratified fluid have been examined by Wu (1969); Schooley and Hughes (1972); Manins (1976); Amen and Maxworthy (1980); Britter and Simpson (1981); Faust and Plate (1984) and Rooij (1999), and the dynamics of bottom-propagating gravity currents in uniformly stratified fluid have recently been examined by Maxworthy et al. (2002) and Ungarish and Huppert (2002). The gravity currents were created (or simulated) using a lock-release initial condition in which uniform fluid within a lock was released into the stratified ambient.

In all these experiments IGW were generated by two mechanisms: first, through the horizontal motion of the intrusion or gravity current forcing the surrounding stratified fluid and second,

through the flow of ambient fluid replenishing the fluid that had left the lock.

One purpose of our experiments was to reduce the effect of the latter generation mechanism by allowing the lock fluid to collapse into a uniform ambient fluid so that the return flow did not directly excite IGW.

The experimental setup is illustrated schematically in Fig. 2. It shows a two-layer fluid whose upper layer has uniform density and whose bottom layer is uniformly stratified. The lock fluid only spans the depth of the upper layer. Once released, the collapsed lock-fluid propagates along the upper interface of a stratified fluid that moves only in local response to the forward-moving intrusion and not in global response to a return flow.

The second purpose for examining dynamics in such a complex two-layer fluid was that it was representative both of the surface mixed layer of the ocean with an underlying thermocline and, upside-down, of the troposphere underlying the stratosphere. The latter scenario is effectively modelled over vertical distances smaller than the local scale-height of the atmosphere because in the Boussinesq approximation downward-propagating IGW obey the same dynamics as upward-propagating IGW. The stratification prescribed by the former, oceanic, scenario was considered by Delisi and Orlanski (1975); Baines (1982); Thorpe (1998) and Gerkema (2001) in studies of nonlinear interactions between vertically propagating internal waves and interfacial waves. However, their work did not consider the dynamics of intrusions or mean flows.

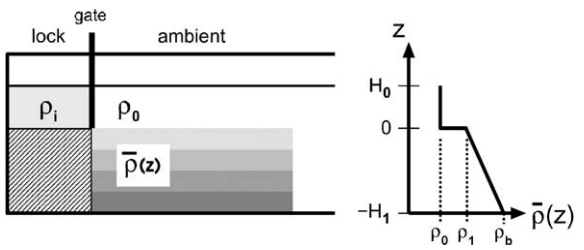

Fig. 2. Schematic of experimental setup showing a lock fluid of density ρ_i behind a gate and overlying a platform (diagonally striped region). The increasing shades of gray to the right of the lock represent the continuous stratification that spans the height of the platform.

Our experiments were performed in a glass tank measuring 197.1 cm long by 19.9 cm wide by 48.5 cm tall. A 30.0 cm tall and 19.6 cm long platform that spanned the width of the tank was installed at one end.

The tank was filled with a two-layer fluid in which the lower layer was stratified and the upper layer had uniform density, as illustrated schematically in Fig. 2. This was established in a two-step process. First, a uniformly stratified fluid was added to the tank using the standard "double bucket" technique (Oster, 1965). The top of this stratified layer was at 30 cm, equal to the level of the top of the platform. Using a sponge-float, a 15.0 cm deep layer of fresh or slightly saline water of density ρ_0 was then layered on top of the uniformly stratified layer.

The resulting density profile was measured using a vertically traversing conductivity probe (Fast Conductivity and Temperature Probe—Precision Measurement Engineering). From the vertical density profile in the lower layer, $\bar{\rho}(z)$, we compute the squared buoyancy frequency $N^2 = -(g/\rho_{00})\,\mathrm{d}\bar{\rho}/\mathrm{d}z$, in which g is the acceleration due to gravity and ρ_{00} is a characteristic density of this Boussinesq fluid. The conductivity probe also measured the density change, $\rho_1 - \rho_0$ and thickness, H_{Int}, of the step between the stratified and uniform fluids. Here ρ_1 is the density of the fluid at the top of the stratified layer. Typically we found $H_{\mathrm{Int}} \simeq 1$ cm.

After filling the tank a 0.4 cm thick gate was inserted between a pair of vertical glass guides and was lowered to the level of the platform near its edge, thus forming a 15 cm deep lock of length $\ell = 18.6$ cm. Salt and a small volume of food-coloring were then added to the lock fluid after which it was mixed vigorously for approximately 15 s. The resulting homogeneous lock fluid had density ρ_i.

In total, 39 experimental runs were performed in which the following three parameters were varied: N^2, $\sigma_{10} = (\rho_1 - \rho_0)/\rho_0$ and $\sigma_{i0} = (\rho_i - \rho_0)/\rho_0$. Experiments were performed with N^2 ranging from 0.37 to 1.21 s^{-2}, σ_{10} ranging from 0.0015 to 0.0102 and σ_{i0} ranging from 0.0005 to 0.0023. In all but

three cases, we set $\sigma_{i0} < \sigma_{10}$ so that the intrusion density matched an isopycnal surface within the interface of the two-layer fluid. Thus we were able to examine the response of the stratified layer beneath the intrusion which, in itself, did not penetrate deeply into the lower layer.

Runs began by rapidly removing the gate from the tank. The lock fluid then collapsed to form an intrusion that propagated along (or in the three cases for which $\sigma_{i0} > \sigma_{10}$, just below) the interface. A CCD camera was used to record the resulting fluid motions. It was placed $L_c = 400\,\mathrm{cm}$ in front of the tank and captured a field of view that covered a horizontal distance $L_w = 87\,\mathrm{cm} \simeq 4.7\ell$. In all cases, the edge of the platform was at the far left extremity of the field of view. Images were analyzed using DigImage (Dalziel, 1992). It was used to convert "snapshot" images of the experiment (having a spatial resolution of approximately $0.2\,\mathrm{cm} \times 0.2\,\mathrm{cm}$) into time series images (having a temporal resolution as small as 1/30 s).

The IGW that appeared in the (stratified) lower layer were visualized using "synthetic schlieren" (Sutherland et al., 1999; Dalziel et al., 2000), a technique that exploits variations in the index of refraction with salinity in order to visualize and measure the deflection of light rays as they travel through stratified fluid of spatially and temporally varying density gradient. By measuring the deflection one can determine the structure and amplitude of the waves continuously and non-intrusively.

Specifically, we measure the value of $\Delta N^2(x, z, t)$, the perturbation to the squared buoyancy frequency, and its time derivative N_t^2. The amplitudes of these fields are themselves proportional to the maximum vertical displacement of the waves, A.

IGW were observed in all but three experiments in which the stratification, $N^2 = 0.37\,\mathrm{s}^{-2}$, was weakest. For these, the absence of observed waves was attributed to the signal from the waves being weaker than the signal noise, for example, due to temperature fluctuations in the laboratory and degradation of the transmitted images. Signal noise is less significant in experiments with stronger stratification because, for a wave of fixed amplitude and spatial structure, the wave signal increases as N^3.

3. Experimental results

3.1. Intrusion analyses

Once released from the lock the gravity current propagates at approximately constant speed, U_i, over the field of view of the camera. This speed was measured from horizontal time series of the digitized experimental images (e.g. see Mehta et al., 2002).

The intrusion speeds measured in all experiments are plotted in Fig. 3A. Here U_i is normalized by a characteristic gravity current speed $C_0 = \sqrt{g\sigma_{i0}H_0}/2$. This is the predicted speed the intrusion would have if it was energy-conserving and if the level $z = 0$ was a rigid bottom (Benjamin, 1968). In the limit $\sigma_{i0} \ll 1$, the intrusion indeed propagates primarily within the uniform density fluid and the underlying stratified fluid acts approximately as a rigid bottom. We expect, and show, that increasing discrepancies in the predicted intrusion speed occur as σ_{i0} increases.

The plot shows that in most experiments the normalized intrusion speed is moderately smaller than 1.0 and that the relative speed generally decreases as σ_{i0} increases. Conversely, Fig. 3B shows that at fixed σ_{i0} (in this case $\simeq 0.0005$) the relative intrusion speed increases as σ_{10} increases. This is true for other values of σ_{i0} we examined. In cases with small σ_{i0}, the speed lies within 10% of the value C_0 and the specific value of N^2 has a relatively small effect on U_i.

We conclude that, at least in the parameter ranges we have examined, the intrusion speed is governed primarily by energy-conserving gravity current dynamics and that deviations from C_0 occur because the intrusion is able to slump below the level $z = 0$ and so effectively reduce its height in the ambient above $z = 0$. Larger σ_{i0} leads to deeper slumping and larger σ_{10} inhibits slumping. These observations are consistent with measurements of the current depths above and below the interface (Flynn and Sutherland, 2004).

The horizontal extent of the intrusion head, l_i, was determined from vertical time series taken

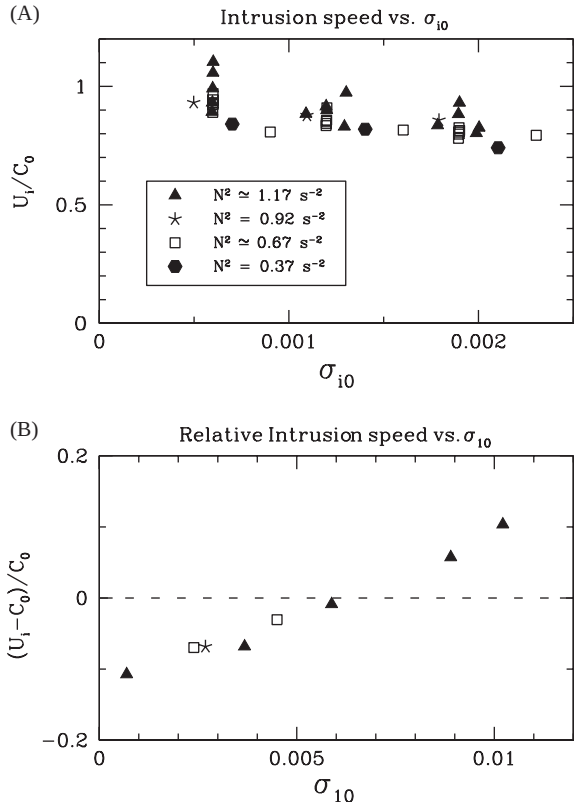

Fig. 3. (A) Normalized gravity current speeds, U_i, as a function of σ_{i0} for all experiments and (B) $U_i - C_0$ as a function of σ_{10} for experiments with small $\sigma_{i0} \simeq 0.0005$. In both plots, the speeds are normalized by $C_0 = (g\sigma_{i0}H_0)^{1/2}/2$. Different symbols are plotted depending on the value of N^2 below $z = 0$, as indicated in the legend.

one lock length from the gate. Specifically, l_i corresponds to the distance between the leading edge of the intrusion and the projected location at which the height of the intrusion head is equal to the height of the trailing tail. It was difficult to measure l_i precisely because the rear of the intrusion head was often obscured by transient billows. Typical measurement errors were 15%.

Knowing U_i and l_i, we estimate the characteristic frequency, ω_i, associated with the forcing on the stratified fluid imparted by the intrusion head by

$$\omega_i = U_i \frac{2\pi}{l_i}. \quad (1)$$

3.2. Internal gravity wave analyses

When the intrusion is released it excites IGW in the stratified fluid beneath it. Synthetic schlieren measures the corresponding ΔN^2 and N_t^2 fields, which are shown for a particular experiment at time $t = 15$ s in Fig. 4. Only the snapshot in the camera's field of view between $x = 25$ and 90 cm is shown. The position $x = 0$ corresponds to the end wall of the tank so that the left extremity of the image is 6.8 cm from the original position of the gate. The vertical range of the images extends from $z = -20$ cm (10 cm above the bottom of the tank) to $z = 0$ cm, the level of the interface between the stratified and unstratified fluid.

As evident from images above $z = 0$ (not shown) the front of the intrusion is situated near $x = 60$ cm at this time. The ΔN^2 field, which is proportional to the change in density gradient, shows a disturbance propagating rapidly upstream just below the level of the interface. IGW propagating downward directly below the intrusion are also evident. ΔN^2 is large near $z = 0$ because the background N^2 is relatively large at the interface. Below the interface ΔN^2 is as large as $0.3\,\mathrm{s}^{-2}$. That is, the background N^2 changes by as much as 25% due to the stretching and compressing of isopycnal surfaces by waves.

Because it takes a time derivative, the N_t^2 field filters slowly varying disturbances and tends to enhance visualisation of vertically propagating IGW rather than long horizontal wavelength (columnar) disturbances. This is evident in Fig. 4B, where downward left-to-right-propagating waves are shown.

The properties of downward-propagating IGW were estimated from equally spaced vertical time series of N_t^2, from which horizontal time series were then constructed. Power spectra were then used to determine the wavenumber, (k_x, k_z), and frequency, ω, of the waves containing most of the energy. In practise we find this peak is quite sharp indicating that the waves are generated within a narrow frequency and wavenumber band (Flynn and Sutherland, 2004).

Fig. 5A plots the measured peak values of frequency and horizontal wavenumber. We do not

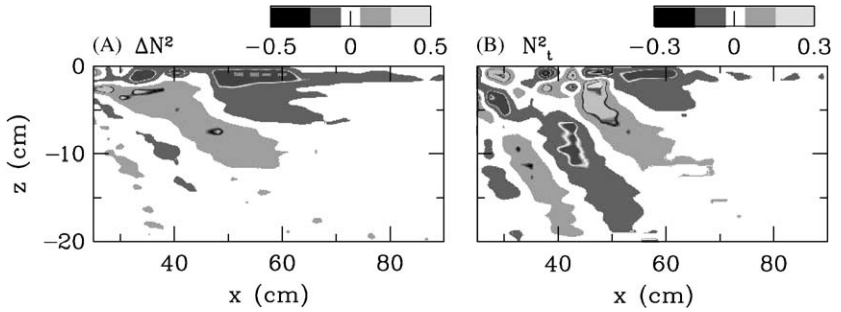

Fig. 4. (A) ΔN^2 and (B) N_t^2 fields at $t = 15\,\mathrm{s}$ in an experiment with $N^2 = 1.17\,\mathrm{s}^{-2}$ below $z = 0$, $\sigma_{10} = 0.0037$ and $\sigma_{i0} = 0.0020$.

plot the vertical wavenumber because the wavelength was found to be smaller than but comparable to the vertical extent of the field of view. This introduced unacceptably large errors in the estimates of k_z. The horizontal wavenumber is plotted normalized by $k_i = 2\pi/l_i$, the estimated wavenumber of the forcing imparted by the intrusion head of length l_i. Likewise the frequency is plotted normalized by $\omega_i = U_i k_i$, the estimated forcing frequency.

The plot shows that k_x is moderately larger than k_i. Although there is quite a bit of scatter in the data, much of this can be attributed to the 15% error associated with the estimate of l_i. We conclude that the extent of the intrusion head is primarily responsible for setting the horizontal scale of the waves.

The plot also shows that ω is consistently larger than ω_i. Indeed, the wave frequency is up to 3 times larger than the equivalent forcing frequency. The scatter in the points in this case well exceeds the associated error bars, and so we conclude that the forcing frequency is not primarily responsible for setting the wave frequency.

Rather it appears that the buoyancy frequency, N, determines the value of ω. This is demonstrated in Fig. 5B. Here we plot the relative amplitude A of the waves against ω/N. We find that the frequency ratio generally lies between values of 0.5 and 0.75 for a wide range of forcing frequencies and values of N. From the linear dispersion relation of IGW, we know $\Theta = \cos^{-1}(\omega/N)$ represents the angle formed by lines of constant phase with the vertical. Thus we find that the waves generally propagate at angles between 41° and 60°.

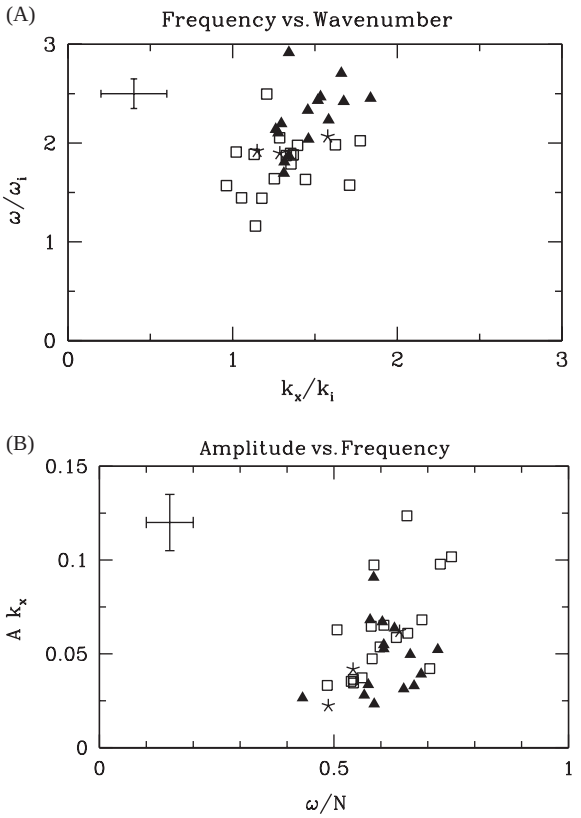

Fig. 5. (A) Measured frequency and wavenumber of IGW expressed as fractions of forcing frequency, $\omega_i = U_i(2\pi/l_i)$, and wavenumber, $k_i = 2\pi/l_i$, respectively. (B) Relative amplitude plotted as a function of wave frequency relative to the background buoyancy frequency. Typical error bars are indicated in the top left-hand corner of both plots. Symbols are plotted as indicated in Fig. 3.

This observation is consistent with Dohan and Sutherland (2003) who found that IGW generated below a turbulent, but stationary, mixed region

propagated within a narrow frequency band. They proposed that when IGW are generated by a fluidic, rather than rigid disturbance, they resonantly interact with the source region in a manner that most strongly excites those waves that vertically transport the most horizontal momentum. These waves, which propagate at angles of about 45°, exert the greatest influence upon the mixing region by exerting the greatest drag to it as a consequence of momentum extraction.

The wave amplitude, A (the maximum vertical displacement), is determined from $A_{N_t^2}$, which in turn is found by computing half the maximum difference between adjacent troughs and crests in vertical time series images of the N_t^2 field. To avoid initial transient effects, the time series were taken one lock-length from the gate. Measurements were typically made 3 cm below the interface. This level was chosen as the approximate position close to the source region but not so close that quantitative schlieren measurements were unreliable due to large isopycnal displacements creating overly distorted images.

4. Numerical simulation setup

The collapse and propagation of the gravity current and the dynamics of the IGW it generates was simulated numerically using a code that solved the fully nonlinear Navier–Stokes and mass-conservation equations in two dimensions. The equations were simplified by invoking the Boussinesq approximation, which assumes that the maximum change of salt-water density from the top to bottom of the tank is negligibly small compared with the density of water itself.

Thus the code solved the following two coupled partial differential equations for the basic-state fields of vorticity, ζ, and perturbation density, ρ':

$$\frac{\partial \zeta}{\partial t} = -u\frac{\partial \zeta}{\partial x} - w\frac{\partial \zeta}{\partial z} + \frac{g}{\rho_{00}}\frac{\partial \rho'}{\partial x} + \nu\nabla^2\zeta \tag{2}$$

and

$$\frac{\partial \rho'}{\partial t} = -u\frac{\partial \rho'}{\partial x} - w\frac{\partial \rho'}{\partial z} - w\frac{\mathrm{d}\,\bar{\rho}}{\mathrm{d}\,z} + \kappa\nabla^2\rho'. \tag{3}$$

Here the horizontal and vertical components of the velocity field were given by u and w, respectively. These were related to the streamfunction, ψ, by $u = -\partial\psi/\partial z$ and $w = \partial\psi/\partial x$, and ψ, in turn was related implicitly to the vorticity field by

$$\zeta = -\nabla^2\psi. \tag{4}$$

Thus, once ζ was determined at a particular time, the Poisson equation, 4, was solved to find ψ from which (u, w) was found and ultimately used in (2) and (3) to determine how the basic-state fields changed in time.

The physical parameters of the system of equations were g, the gravitational acceleration, ρ_{00}, the characteristic density, ν, the kinematic viscosity, and κ, the diffusivity of salt water. Assuming weakly saline solutions, we took each of these to be constant. Specifically, $g = 980\,\mathrm{cm/s^2}$, $\rho_{00} = 1\,\mathrm{g/cm^3}$, $\nu = 0.01\,\mathrm{cm^2/s}$ and $\kappa = 0.01\,\mathrm{cm^2/s}$. The last of these was unphysical; $10^{-5}\,\mathrm{cm^2/s}$ would have been more appropriate for the diffusivity of salt water. If we used this value, however, the simulation would have been numerically unstable. For the purposes of simulating the experiments, the diffusivity term in 3 acted solely as a filter to damp small-scale numerical noise. The value we used was still sufficiently small that the essential dynamics of the gravity current's propagation and wave generation were not affected.

The code was originally designed to model the evolution of unstable stratified parallel flows (Smyth and Peltier, 1991), and so it solved the equations in a L-long by H-deep domain which was a horizontally periodic channel with free-slip upper and lower boundary conditions.

To adapt the code to model the experiment described in Section 2, we chose a computational domain with twice the horizontal extent of the tank (i.e. $L = 2L_T$) and we prescribed initial conditions with reflection symmetry about the mid-vertical plane of the domain. We confirmed, a posteriori that indeed there was no significant motion across this reflection plane nor across the right and left-extremes of the domain. Hence, the right-half of the domain simulated the dynamics of a gravity current bounded on four sides by free-slip boundaries. Simulations were run with $H = H_T = H_0 + H_1$, the depth of the tank, and with

$H = 4H_T$. The latter enabled us to simulate the experiment while eliminated the effect of bottom reflection of the IGW over the duration of interest.

Initial conditions for a particular simulation are shown in Fig. 6. The right-hand plots show the initial profiles of the background density, $\bar{\rho}(z)$ and the corresponding squared buoyancy frequency $N^2(z)$. Explicitly,

$$N^2(z) = \begin{cases} N_0^2, & 0 \leqslant z \leqslant H_0, \\ N_{\rm Int}^2, & -H_{\rm Int} \leqslant z < 0, \\ N_1^2, & -H_1 \leqslant z < -H_{\rm Int}. \end{cases} \quad (5)$$

In particular, as illustrated in Fig. 6, when $N_0^2 = 0$ the background density was constant ($= \rho_0$) over the top H_0 of the domain. Below a $H_{\rm Int} = 1$ cm deep interface the density increased linearly as characterized by a constant squared buoyancy frequency equal to N_1^2. Across the interface the relative density increased by σ_{10}, which was written in terms of $N_{\rm Int}^2$ by $\sigma_{10} = H_{\rm Int} N_{\rm Int}^2/g$.

As well as the profiles shown, we ran simulations with $N^2(z) = N_1^2$ everywhere and with $N^2(z) = N_1^2$ above and below a $H_{\rm Int} = 1$ cm deep interface with the density increasing linearly with depth by $\rho_1 - \rho_0 = 0.0037\,{\rm g/cm^3}$ across the interface.

These profiles determined the density structure at every horizontal position along the domain. In addition, we superimposed an initial density perturbation such that

$$\rho'(x, z, t = 0) = \begin{cases} \rho_i, & |x| < \ell, 0 \leqslant z \leqslant H_0, \\ 0, & \text{otherwise.} \end{cases} \quad (6)$$

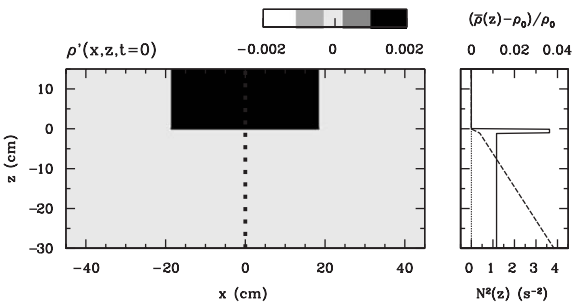

Fig. 6. Perturbation density field (left), ambient density profile (right dotted) and N^2 profiles (right, solid) used to initialize the numerical simulations.

The density perturbation field is shown by color contours on the left-hand side of Fig. 6 for the case $\rho_i = 0.0020\,{\rm g/cm^3}$ and $\ell = 18.6$ cm. Here, only a window within the actual domain size is shown.

Because of the additional complexity involved with the numerics, the simulation did not model the effect of a rigid boundary beneath the lock fluid. Rather, stratified ambient fluid underlies the lock and is free to move in response to the collapse of fluid in the lock. The simulations thus enable us to examine the effect of this response to wave generation.

The details of the numerical representation of the basic-state equations are given by Sutherland and Peltier (1994). Here we ran simulations with a typical horizontal and vertical resolution of 0.2 and 0.06 cm, respectively. The time step was 0.005 s.

5. Simulation results

5.1. Direct simulation of a laboratory experiment

We have run simulations using parameters nearly identical to that of the particular laboratory experiment, shapshots of which are shown in Fig. 4. Explicitly, we initialize the simulation with an ambient N^2 profile given by 5 with $N_0^2 = 0$, $N_{\rm Int}^2 = 3.63\,{\rm s^{-2}}$, $N_1^2 = 1.17\,{\rm s^{-2}}$ and with $H_0 = 15$ cm, $H_{\rm Int} = 1$ cm and $H_T = 45$ cm. The buoyancy frequency at the interface ($-1 \leqslant z < 0$) corresponds to a relative density increase of $\sigma_{10} = 0.0037$. An initial density perturbation is given by (6) with $\rho_i = 0.0020\,{\rm g/cm^3}$. This is applied in a rectangular region bounded by $0 \leqslant z \leqslant H_0$ and $|x| \leqslant \ell$.

Snapshots taken from this simulation of the perturbation density and vorticity fields are shown in Fig. 7. Though the total horizontal extent of the computational domain is $|x| < L_T$ with $L_T = 197.1$ cm, only the range $0 \leqslant x \leqslant 90$ is shown. The images clearly show that the lock fluid collapses to form an intrusive gravity current that propagates along the interface between the upper uniform density ambient and the lower stratified ambient fluid. Consistent with experiments, Kelvin–Helmholtz billows develop behind the head of

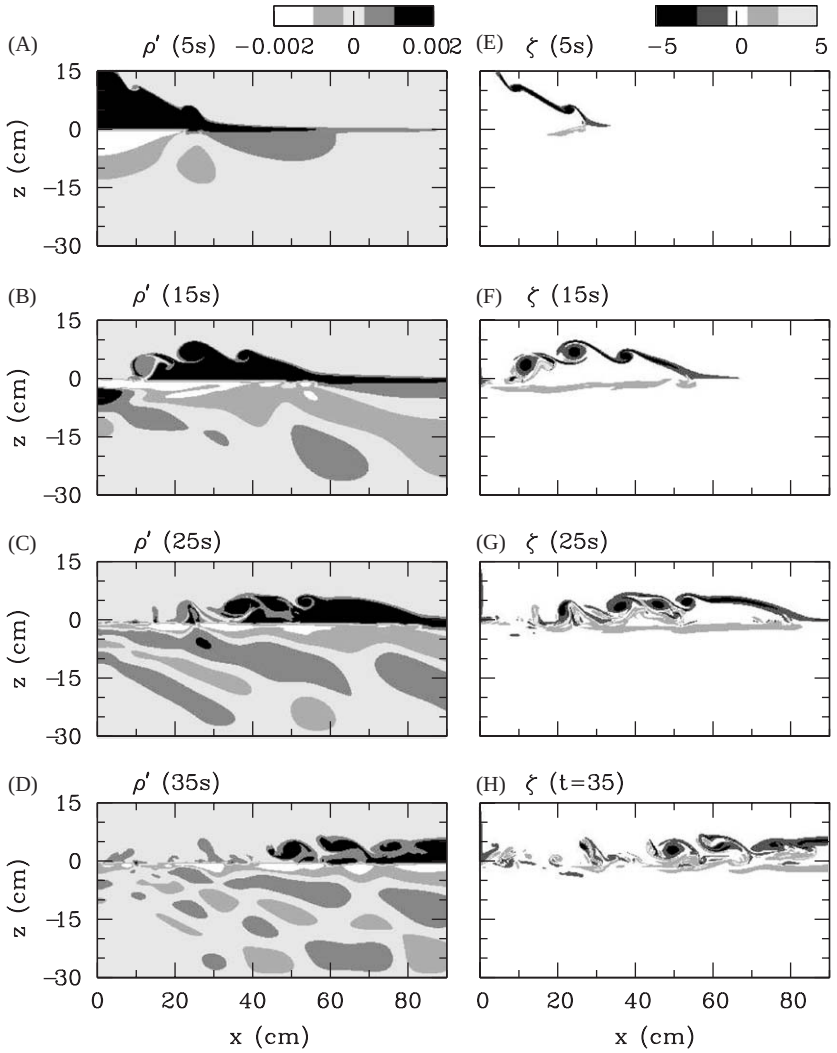

Fig. 7. Snapshots from numerical simulation with $N_0^2 = 0$, $N_1^2 = 1.17\,\mathrm{s}^{-2}$, $\sigma_{10} = 0.0037$ and $\sigma_{i0} = 0.0020$. The perturbation density field ρ', like σ_{i0}, is given in nondimensional units. The vorticity field ζ' is given in units of s^{-1}.

the intrusion on its upper flank, but such instability is not apparent on its lower flank. The mixing occurs primarily behind the head of the intrusion so that the density near the nose of the intrusion remains constant. Likewise, the vorticity field remains zero near the nose except on thin sheets surrounding the gravity current head. Thus, consistent with the experimental observations of Lowe et al. (2002), the velocity near the nose of the current is approximately constant.

IGW are excited immediately after the fluid begins to collapse. The waves transport energy down and rightward until they reflect off the bottom at $z = -30$. This reflection is evident at $t = 25\,\mathrm{s}$ after which time the wave field exhibits a complicated pattern of interference between downward and upward propagating waves.

We have performed a simulation (not shown) in which all parameters are identical to those in the above simulation except that we quadruple the

depth of the domain while keeping the vertical resolution the same. This simulation gives the same results at early times, but reflection does not corrupt the wavefield at $t = 25$ s.

Corresponding to Figs. 7B and F, Fig. 8 plots the ΔN^2 and N_t^2 fields at $t = 15$ s. For comparison with the experimental results shown in Fig. 4, the fields are shown only for $25 \leqslant x \leqslant 90$ and $-20 \leqslant z \leqslant 0$.

Both the simulations and experiments show left-to-right downward-propagating IGW emanating from the head of the intrusion whose front is near $x = 60$ cm. However, the amplitude of the simulated ΔN^2 field is almost twice that measured in experiments. Furthermore, whereas in the experiments a regular pattern of waves is evident in the N_t^2 field (Fig. 4B), no such regularity is evident in the simulated field. Rather the lines of constant phase vary from nearly vertical to nearly horizontal and the waves themselves appear to emanate from a localized source near $(x, z) \simeq (55\,\text{cm}, -2\,\text{cm})$.

We attribute these discrepancies to the fact that the simulations do not include the effect of a rigid bottom boundary directly beneath the lock as would be present due to the platform employed in the experiments. Fig. 7A shows that, without the platform, fluid beneath the lock is displaced downward during the initial collapse phase. The associated values of ΔN^2 at this location (not shown) are an order of magnitude larger than those associated with waves in the experiments. This could explain in part the occurrence in the simulations of large-amplitude disturbances of long horizontal extent at $t = 15$ s (Fig. 8A). Supporting this assertion, we find that the N_t^2 field (which filters long-time scale shallow motions) has comparable simulated and experimental amplitude for the primary wave (shown by light-gray contours) below the intrusion front.

The structure of the waves in the two cases is nonetheless different. We attribute the discrepancy to the approximately horizontal flow induced by the initial displacement of fluid below the lock in simulations. This flow effectively Doppler shifts the transmitted waves and prevents them from being transmitted far away from the source. Indeed this Doppler shifting is apparent in the waves shown in Fig. 8B. The primary wave and trailing trough have nearly vertical phase lines for $-10 \leqslant z \leqslant -5$ but these become more shallow below $z \simeq -10$ cm. Further behind the intrusion front, the waves generated by the source are sufficiently Doppler-shifted that the waves are evanescent. Diagnosis of the horizontal velocity field at $t = 15$ s (not shown) reveals that the flow speed decreases by approximately 2 cm/s from $z = 0$ to -5 cm. For waves with horizontal wavenumber $2\pi/20\,\text{cm}^{-1}$ and intrinsic frequency $0.6N$ (typical values taken from experimental data), the Doppler-shifted frequency at $z = -5$ cm would be $1.2N$, which demonstrates that the waves are indeed evanescent.

These simulations thus serve to demonstrate that the mechanism for wave generation sensitively depends upon the flow in the ambient. This observation is consistent with the conclusions by Hughes (1996) who examined in experiments the collapse of a mixed region in a uniformly stratified

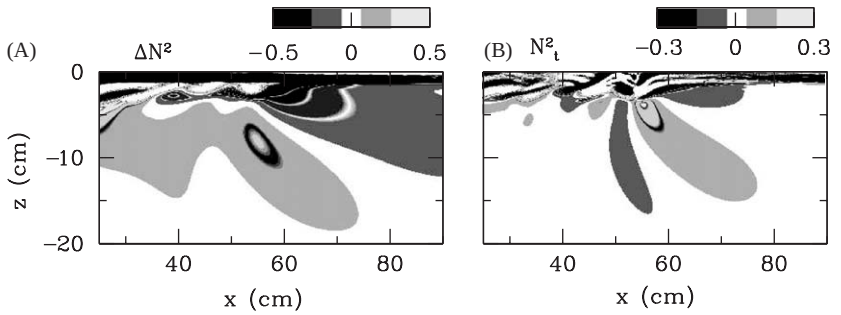

Fig. 8. Snapshots of (A) ΔN^2 and (B) N_t^2 fields at $t = 15$ s in a simulation with the same parameters as those given in Fig. 7.

fluid. He found that vertically propagating IGW were prevented from propagating away from the intrusions on either side of the mixing region because the return flow above and below the intrusion had sufficiently large velocity to Doppler-shift waves to evanescent frequencies.

5.2. Simulation of uniformly stratified ambient

One reason for the relatively complicated experimental setup we have used is that we wanted the lock-fluid to collapse within an ambient fluid of uniform density over the depth of the lock so that the process of lock-collapse and, in particular, the development of a return flow into the lock would not in itself directly excite IGW. IGW can only be excited as a consequence of the intrusion moving along the interface above a stationary stratified ambient.

In order to demonstrate the effect of a lock-fluid collapsing in a stratified ambient we present here the results of two simulations which are simple extensions of the simulation described in Section 5.1.

In both, we set the ambient fluid to be uniformly stratified with $N^2 = 1.17\,\mathrm{s}^{-2}$ both above $z = 0$ and below $z = -H_{\mathrm{Int}}$. For $-H_{\mathrm{Int}} \leqslant z < 0$, the stratification is the same as before. A density perturbation is introduced in a model lock above $z = 0$ and for $|x| < \ell$.

In one simulation, the lock has the same stratification as the ambient, but a density perturbation of $\rho_i = 0.0020\,\mathrm{g/cm}^3$ is superimposed. The results of this simulation are shown in Fig. 9, and should be compared with the top four images in Fig. 7. The perturbation density field at times 5 and 15 s (Figs. 9A and B, respectively) demonstrates notably different behavior from that in the simulation with a uniform ambient. Here the density anomaly does not remain concentrated in a collapsing current. Rather, it creates a disturbance that propagates rapidly to the right at the same vertical level as the lock. After 15 s the perturbation density field is characterized by IGW throughout the domain. No sharp front, as one would associate with a gravity current head, is evident. Likewise the vorticity field (Figs. 9C and D, respectively) exhibits no characteristic traits of Kelvin–Helmholtz instability. Indeed, the vorticity field is significantly weaker as evident from the range of grayscale which is five times smaller than that used to plot Figs. 7E and F.

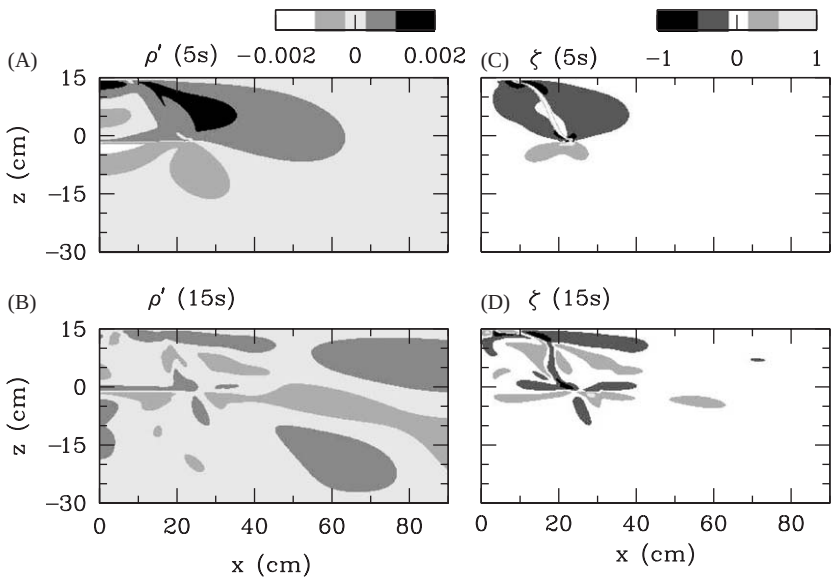

Fig. 9. Snapshots from a numerical simulation with an almost uniformly stratified ambient (see text) and with a lock-fluid having the same density gradient as the ambient but with a density difference $0.0020\,\mathrm{g/cm}^3$ at each vertical level in the lock.

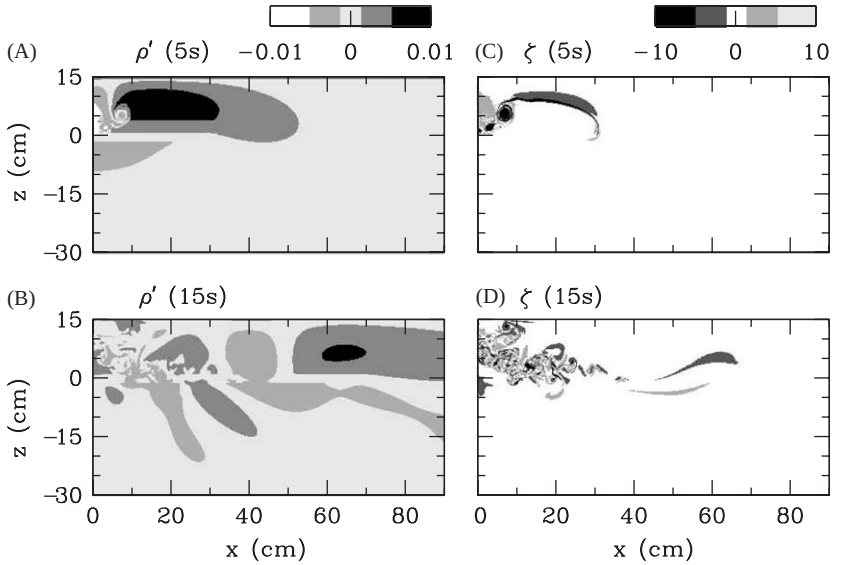

Fig. 10. Snapshots from a numerical simulation with an almost uniformly stratified ambient (see text) and with a uniform initial lock-fluid density.

In a second simulation, the lock has uniform density which is greater than the density of the ambient at $z = 0$ by $0.0020\,\mathrm{g/cm^3}$. The results of this simulation is shown in Fig. 10. Again a collapsing gravity current head is not evident. Rather, IGW are found to propagate rapidly to the right. The vorticity field is stronger in this case due to baroclinically generated negative vorticity in the lock during the initial stages of collapse (Fig. 10c). However, the initially coherent vortices are rapidly broken down into smaller-scale structures in the lock after 15 s.

Both simulations show that the flow dynamics change qualitatively when the ambient fluid throughout the depth of the lock is stratified rather than unstratified.

6. Application to surface mixed region

Here we adapt the experimental results in order to form order-of-magnitude estimates of the momentum flux associated with waves generated by intrusions propagating in the surface mixed region above the thermocline. The approach is analogous to that taken by Flynn and Sutherland (2004) in their study of IGW generated in the stratosphere by thunderstorm outflows below the tropopause.

The ability of IGW to vertically transport horizontal momentum is characterized by the average Reynolds stress, $\rho_{00}\langle uw\rangle$. This in turn can be related to experimental parameters in an empirically determined formula (Flynn and Sutherland, 2004):

$$\frac{\rho_{00}\langle uw\rangle}{(N_1 l_i)^2} = 10^{-3.7\pm0.3}\rho_{00}\left(\frac{U_i}{\sqrt{\sigma_{10} g h_i}}\right)^{2.9\pm0.6}. \qquad (7)$$

The exponents with associated errors are determined from the slope and intercept of the best-fit line through log–log plots of momentum flux and current speed measurements gathered from 30 experiments. Here h_i is the total height of the intrusion head, which observations show can be related to the length of the head by $l_i \simeq 4.7 h_i$.

Because there are no direct observations of intrusions above the thermocline, we must estimate values of the parameters in (7) in order to form an estimate for the momentum flux. We do so by focusing on a particular geophysical event: the passage of Hurricane Norbert over the eastern north Pacific Ocean during September and October of 1984. The observations and simulations

of Price et al. (1994) give estimates of the surface cooling and mixed layer deepening due to this storm. As a result of storm-induced vertical mixing, they predict a deepening of the surface mixed layer from 50 m to approximately 90 m and a corresponding mixed layer density increase of approximately $0.64\,\mathrm{kg/m^3}$.

Relative to the unperturbed ambient, we speculate that this mixed parcel of fluid ultimately collapses and propagates as a fluid intrusion at a depth $z_{\mathrm{NB}} = -58.4\,\mathrm{m}$. The intrusion's plane of propagation is therefore directly below the level $z = -50\,\mathrm{m}$, which denotes the bottom of the uniform ambient mixed region.

To estimate the relevant parameters associated with this intrusion, we define σ_{10} such that

$$\sigma_{10} = \frac{Ch_i}{\rho_{00}}\left(-\frac{\mathrm{d}\bar{\rho}}{\mathrm{d}z}\right), \tag{8}$$

where $-\mathrm{d}\bar{\rho}/\mathrm{d}z$ is the ambient density gradient between $z = -50\,\mathrm{m}$ and $-90\,\mathrm{m}$ and

$$C = \min\left[\frac{(z_{\mathrm{NB}} - z_0) + h_1}{h_i}, 1\right]. \tag{9}$$

Here $z_0 = -50\,\mathrm{m}$ and h_1 is the intrusion's depth of penetration into the (lower) stratified layer. The constant, C, is defined so that σ_{10} represents the magnitude of the normalized density jump across a distance Ch_i.

We further relate h_i and σ_{10} using the first-order perturbation approximations for the intrusion height in a two-layer model (Holyer and Huppert, 1980; Flynn and Sutherland, 2004). Thus we find

$$\frac{h_i}{z_{\mathrm{NB}}} = \frac{1}{2} + \frac{5}{32}\left(\frac{\sigma_{i0}}{\sigma_{10}}\right). \tag{10}$$

In the wide range of experiments by Flynn and Sutherland (2004), this estimate was found to be moderately smaller than the observed heights, but was sufficiently close that its use here is appropriate to determine order-of-magnitude momentum flux estimates. Eqs. (8)–(10) are solved using a simple iterative routine from which we find $\sigma_{10} \simeq 0.0010$. A posteriori this value of σ_{10} is sufficiently small that such an order-of-magnitude estimate is self-consistent.

Using this value of σ_{10}, we predict the vertical and horizontal extent of the intrusion head to be $h_i \simeq 35.1\,\mathrm{m}$ and $l_i \simeq 166\,\mathrm{m}$, respectively. We estimate the propagation speed from the first-order perturbation expansion of the predicted steady-state intrusion speed in a two-layer fluid (see Eq. (2.8) of Flynn and Sutherland, 2004). The normalized speed of propagation is thereby determined to be $U_i/\sqrt{\sigma_{10} g h_i} \simeq 0.5$, and so we find $\rho_{00}\langle uw\rangle$ ranges between 0.2 and $2\,\mathrm{N/m^2}$.

By comparison, IGW excited below the mixed region of the equatorial Pacific were observed to have typical Reynolds stress values of approximately $0.3\,\mathrm{N/m^2}$ (Lien et al., 1996), and Wijesekera and Dillon (1991) estimated that for narrow-band, dynamically generated IGW, the associated Reynolds stress ranged from 0.1 to $0.6\,\mathrm{N/m^2}$.

The above results suggest that the local influence of IGW excited by fluid intrusions is roughly comparable to those generated by other near-surface mechanisms. Globally, however, their significance is likely to be small because severe storms of sufficient energy to substantially deepen the surface mixed layer are relatively intermittent.

7. Conclusions

We have shown that intrusions which propagate over the thermocline can act locally as a significant source of IGW. However, the momentum flux associated with the waves and, indeed, whether the waves are generated at all depends sensitively upon the flow speed of the stratified fluid. Whether from the initial transient collapse of a mixed region into the stratified fluid below or from the horizontal flow of stratified fluid into a collapsing mixed region, long horizontal scale disturbances can be excited. These propagate rapidly away from the source and can filter vertically propagating waves.

We have adapted our experimental results to the ocean surface, but it is evident that IGW generation from a collapsing mixed region would likewise occur in the abyssal ocean. Such mixing could result directly from turbulence generated by flow over rough topography or indirectly from the breaking of inertia gravity waves. In either case, our simulations show that a mixed region in a stratified ambient does not collapse in the form of a standard interfacial gravity current. Rather it

excites IGW of such large amplitude that the mixed region is itself significantly distorted by the waves. The details of these dynamics including the long-term effects of rotation are presently under investigation.

Acknowledgements

This work was financially supported by NSERC's PGS A and Discovery Grants programs, the Killam Trust, Alberta's iCore Program and by the Canadian Foundation for Climate and Atmospheric Sciences (CFCAS).

References

Amen, R., Maxworthy, T., 1980. The gravitational collapse of a mixed region into a linearly stratified solution. Journal of Fluid Mechanics 96, 65–80.

Baines, P.G., 1982. On internal tide generation models. Deep-Sea Research 29, 307–338.

Balmforth, N.J., Ierley, G.R., Young, W.R., 2002. Tidal conversion by subcritical topography. Journal of Physical Oceanography 32 (10), 2900–2914.

Benjamin, T.B., 1968. Gravity currents and related phenomena. Journal of Fluid Mechanics 31, 209–248.

Beres, J.H., Alexander, M.J., Holton, J.R., 2002. Effects of tropospheric wind shear on the spectrum of convectively generated gravity waves. Journal of Atmospheric Sciences 59, 1805–1824.

Britter, R.E., Simpson, J.E., 1981. A note on the structure of the head of an intrusive gravity current. Journal of Fluid Mechanics 112, 459–466.

Cornillon, P., Stramma, L., Price, J.F., 1987. Satellite measurements of sea surface cooling during Hurricane Gloria. Nature 326, 373–375.

Dalziel, S.B., 1992. Decay of rotating turbulence: some particle tracking experiments. Applied Scientific Research 49, 217–244.

Dalziel, S.B., Hughes, G.O., Sutherland, B.R., 2000. Whole field density measurements. Experiments in Fluids 28, 322–335.

Delisi, D.P., Orlanski, I., 1975. On the role of density jumps in the reflexion and breaking of internal gravity waves. Journal of Fluid Mechanics 69, 445–464.

Dillon, T.M., Moum, J.N., Chereskin, T.K., Caldwell, D.R., 1989. Zonal momentum balance at the equator. Journal of Physical Oceanography 19, 561–570.

Dohan, K., Sutherland, B.R., 2003. Internal waves generated from a turbulent mixed region. Physics of Fluids 15, 488–498.

Faust, K.M., Plate, E.J., 1984. Experimental investigation of intrusive gravity currents entering stably stratified fluids. Journal of Hydraulic Research 22 (5), 315–325.

Flynn, M.R., Sutherland, B.R., 2004. Intrusive gravity currents and internal wave generation in stratified fluid. Journal of Fluid Mechanics 514, 355–383.

Garrett, C., St. Laurent, L.C., 2002. Aspects of deep ocean mixing. Journal of Oceanography 58, 11–24.

Gerkema, T., 2001. Internal and interfacial tides: beam scattering and local generation of solitary waves. Journal of Marine Research 59, 227–255.

Hebert, D., Moum, J.N., Paulson, C.A., Caldwell, D.R., Chereskin, T.K., McPhaden, M.J., 1991. The role of the turbulent stress divergence in the equatorial Pacific zonal momentum balance. Journal of Geophysical Research 96 (C4), 7127–7136.

Holyer, J.Y., Huppert, H.E., 1980. Gravity currents entering a two-layer fluid. Journal of Fluid Mechanics 100, 739–767.

Hughes, G.O., 1996. Aspects of mixing in stratified flows. Ph.D. Thesis, University of Cambridge.

Ledwell, J.R., Montgomery, E., Polzin, K., St. Laurent, L.C., Schmitt, R., Toole, J., 2000. Evidence for enhanced mixing over rough topography in the abyssal ocean. Nature 403, 179–182.

Lien, R.-C., McPhaden, M.J., Gregg, M.C., 1996. High-frequency internal waves at 0°, 140° W and their possible relationship to deep-cycle turbulence. Journal of Physical Oceanography 26, 581–600.

Lowe, R.J., Linden, P.F., Rottman, J.W., 2002. A laboratory study of the velocity structure in an intrusive gravity current. Journal of Fluid Mechanics 456, 33–48.

Manins, P.C., 1976. Intrusion into a stratified media. Journal of Fluid Mechanics 74, 547–560.

Maxworthy, T., Leilich, J., Simpson, J., Meiburg, E.H., 2002. The propagation of a gravity current in a linearly stratified fluid. Journal of Fluid Mechanics 453, 371–394.

Mehta, A., Sutherland, B.R., Kyba, P.J., 2002. Interfacial gravity currents: Part II—wave excitation. Physics of Fluids 14, 3558–3569.

Michaelian, M.E., Maxworthy, T., Redekopp, L.G., 2002. The coupling between turbulent penetrative convection and internal waves. European Journal of Mechanics B 21, 1–28.

Moum, J.N., Hebert, D., Paulson, C.A., Caldwell, D.R., 1992. Turbulence and internal waves at the equator. Part 1: Statistics from towed thermistors and a microstructure profiler. Journal of Physical Oceanography 22, 1330–1345.

Oster, G., 1965. Density gradients. Scientific American 213, 70.

Price, J.F., Sanford, T.B., Forristall, G.Z., 1994. Forced stage response to a moving hurricane. Journal of Physical Oceanography 24, 233–260.

Rooij, F. de, 1999. Sedimenting particle-laden flows in confined geometries. Ph.D. Thesis, University of Cambridge.

Schooley, A.H., Hughes, B.A., 1972. An experimental and theoretical study of internal waves generated by the collapse of a two-dimensional mixed region in a density gradient. Journal of Fluid Mechanics 51, 159–175.

Skyllingstad, E.D., Denbo, D.W., 1994. The role of internal gravity waves in the equatorial current system. Journal of Physical Oceanography 24, 2093–2110.

Smith, S.G.L., Young, W.R., 2002. Conversion of the barotropic tide. Journal of Physical Oceanography 32, 1554–1566.

Smyth, W.D., Moum, J.N., 2002. Shear instability and gravity wave saturation in an asymmetrically stratified jet. Dynamics of Atmospheres and Oceans 35 (3), 265–294.

Smyth, W.D., Peltier, W.R., 1991. Instability and transition in finite-amplitude Kelvin–Helmholtz and Holmboe waves. Journal of Fluid Mechanics 228, 387–415.

St. Laurent, L.C., Toole, J.M., Schmitt, R.W., 2001. Buoyancy forcing by turbulence above rough topography in the abyssal Brazil Basin. Journal of Physical Oceanography 31, 3476–3495.

Sutherland, B.R., 1996. The dynamic excitation of internal gravity waves in the equatorial oceans. Journal of Physical Oceanography 26, 3214–3235.

Sutherland, B.R., 2002. Large-amplitude internal wave generation in the lee of step-shaped topography. Geophysical Research Letters 29(16), art. no 1769.

Sutherland, B.R., Linden, P.F., 1998. Internal wave generation by flow over a thin barrier. Journal of Fluid Mechanics 377, 223–252.

Sutherland, B.R., Peltier, W.R., 1994. Turbulence transition and internal wave generation in density stratified jets. Physics of Fluids A 6, 1267–1284.

Sutherland, B.R., Dalziel, S.B., Hughes, G.O., Linden, P.F., 1999. Visualisation and measurement of internal waves by "synthetic schlieren". Part 1: Vertically oscillating cylinder. Journal of Fluid Mechanics 390, 93–126.

Thorpe, S.A., 1998. Nonlinear reflection of internal waves at the density discontinuity at the base of a mixed layer. Journal of Physical Oceanography 28, 1853–1860.

Ungarish, M., Huppert, H.E., 2002. On gravity currents propagating at the base of a stratified fluid. Journal of Fluid Mechanics 458, 283–301.

Wijesekera, H.W., Dillon, T.M., 1991. Internal waves and mixing in the upper equatorial Pacific ocean. Journal of Geophysical Research 96, 7115–7126.

Wu, J., 1969. Mixed region collapse with internal wave generation in a density stratified medium. Journal of Fluid Mechanics 35, 531–544.